Microchemical Journal 218 (2025) 115770

Contents lists available at ScienceDirect

Microchemical Journal

journal homepage: www.elsevier.com/locate/microc

Integrating experimental validation, density functional theory insights, and AI perspectives to develop an efficient electrocatalyst for sustainable electricity generation☆

Senthilkumar Nangan [a,*], Yogapriya Selvaraj [a], Manunya Okhawilai [b,*], Anbazhagan Venkattappan [a], Anuj Kumar [c,e], Mohd Ubaidullah [d]

[a] *Center for Research and Development (CRD), Department of Chemistry, Vinayaka Mission's Kirupananda Variyar Arts and Science College, Vinayaka Missions Research Foundation (Deemed to be University), Salem 636308, Tamil Nadu, India*
[b] *Department of Chemical Engineering, Faculty of Engineering, Chulalongkorn University, Bangkok 10330, Thailand*
[c] *Nano-Technology Research Laboratory, Department of Chemistry, GLA University, Mathura, Uttar Pradesh 281406, India*
[d] *Department of Chemistry, College of Science, King Saud University, P.O. Box 2455, Riyadh 11451, Saudi Arabia*
[e] *State Key Laboratory of Chemical Resource Engineering, Beijing Advanced Innovation Center for Soft Matter Science and Engineering, College of Chemistry, Beijing University of Chemical Technology, Beijing 100029, China*

ARTICLE INFO

Keywords:
Urea fuel cell
Artificial intelligence
Urea oxidation
$NiMoO_4$
MXene

ABSTRACT

Reaching two birds with one stone strategy, capable of addressing two issues with a single substance, has been widely deployed in electrochemical fields. Herein, nickel molybdate ($NiMoO_4$) nanorods-decorated Ti_3C_2 MXene (MX) ($NiMoO_4$@MX) is prepared and applied as electrode for electrochemical oxidation reactions of urea and urine samples. Further, the $NiMoO_4$@MX_1 is exploited as self-supporting anode in direct urea fuel cell (DUFC) attaining the maximum power density of 35.4 mW cm^{-2}. Additionally, real samples of human and cow urines are used as the fuel for DUFC and acheving power densities of 29.8, and 27.9 mW cm^{-2}, respectively. At the end of fuel cell operation, 94 and 92 % of urea in human and cow urine, respectively, are removed from DUFC. The underlying reaction mechanism behind the UOR was analyzed with density functional theory (DFT) computation, disclosing the existing adsorption energies and electronic interactions at the $NiMoO_4$@MX_1 interfaces. To strengthen this study, a possible intergration of artificial intelligence (AI)-driven smart computing stratigies with DFT descriptors was discussed, opening a new path toward AI assisted sustainable energy generation.

1. Introduction

The increasing global energy demand, rapid deprivation of fossil fuels, and increased CO_2 emission impacted adverse effect in the last few years globally due to increased population and industrialization. Fuel cells, with their high-energy output, continuous energy supply, and zero-emission footprint have emerged as promising candidates to address these energy scarcities [1]. Direct urea fuel cells (DUFCs) that can produce electricity through oxidation of urea is considered as a promising technology for next-generation energy devices. Because of the utilization of urea as a fuel, urea assisted electricity generation existed as a cost-efficient way along with another favor that mitigates the water eutrophication issues experienced by the discharge of urea-rich wastewater from industries and human/animal urine [2]. Among various reactions, urea assisted water electrolysis considered as a promising technology due to thier lower oxidation potentials, higher current densties enabling the more effcient and cost effective alternative platform for the next-generation clean and green energy productions. In the DUFC, electrochemical urea oxidation reaction (UOR) is a prime half reaction responsible for the facile and effecient electricity generation. The urea oxidation process achieved over redox-active metal centres M^{x+}/M^{y+} (where M- transition metal, x & y – oxidation states), where reversible cycling between oxidation states, promotes the more effecint electron transfer [2,3]. For example, nickel (Ni) and Ni-based materials are widely used as the electrocatalysts for UOR. During this UOR process Ni^{2+}/Ni^{3+} redox couple in alkaline media plays pivotal role for the

---

☆ This article is part of a Special issue entitled: 'AI-based smart intelligence' published in Microchemical Journal.

* Corresponding authors.

E-mail addresses: nskumarchemist91@gmail.com (S. Nangan), manunya.o@chula.ac.th (M. Okhawilai).

https://doi.org/10.1016/j.microc.2025.115770
Received 2 September 2025; Received in revised form 11 October 2025; Accepted 13 October 2025

facilitating charge-transfer kinetics in the metal active centres [4–6]. In addition to DUFC, Ni^{2+}/Ni^{3+} redox couples are also involved in various alkaline fuel cells such as alkaline direct glucose fuel cell to perform anodic electrochemical oxidation reactions [7,8].

Under alkaline conditions, Ni is initially oxidized into Ni^{2+} ($Ni(OH)_2$) and further oxidized to Ni^{3+} (NiOOH) at higher oxidation potentials [4,5,7,8]. In the case of UOR, the generated Ni^{3+} oxidizes urea into CO_2, N_2 and H_2O, while itself is regenerated to Ni^{2+}. Consequently, the DUFC generates electricity during the successive oxidation of urea along with reproduction of Ni^{2+} [4,5,7,8]. Although the oxidation reaction of urea in realtime urine waste follows similar route in the presence of Ni and Ni-based materials, no electrocatalyst with bifunctional activity has been reported to simultaneously evaluate the efficiencies of DUFC under the presence of urea and urine waste samples. Hence, the development of bifunctional electrocatalysts that can be applied to both urea and urine waste samples is not only useful for electricity generation, but also supports to decrease the overall expenditure of DUFC fabrication.

Recently, Ni-based binary transition metal oxides have been explored as electrocatalyst for various electrochemical applications, owing to their excellent electrocatalytic properties [9–13]. Among the existing binary transition metal oxides, the mixed valance state $NiMoO_4$ being inspired in UOR applications due to the synergism of outstanding electrochemical activity of Ni and good electrical conductivity of Mo [14,15]. Although there are a few works reported on $NiMoO_4$, the unsatisfactory outcomes in terms of low exposure of active sites, poor durability because of structural degradation, utilization of high cost substrate, and time consuming fabrication have deteriorated its research attention [14,15].

Inspired by binary transition metal electrocatalysts and concerning the above disputes, we scrupulously designed a free-standing electrode of $NiMoO_4$-anchored titanium (IV) carbide (Ti_3C_2) MX hetero-structure ($NiMoO_4$@MX_1). MXene, an emerging two-dimensional (2D) material, possess high electrical conductivity (~ 24,000 S cm^{-1}), abundant surface functional groups, flexible layered morphology, tunable electronic properties, providing better electron transfer efficiency, uniform metal oxide interfacial bonding, stable electrochemically active metal oxide/MXene heterojunction formation. Hence, herein, the MX sheet is utilized as a catalyst support owing to its functional attributes such as excellent hydrophilicity, high volumetric capacitance, good mechanical stability, and high surface area which provides the excellent catalytic performance [16,17]. The fabricated $NiMoO_4$@MX_1 film exploited as an efficient electrode for UOR, for first time, toward the electrochemical oxidation of urea in human urine and cow urine. Furthermore, the electrochemical efficiency of $NiMoO_4$@MX_1 film for the efficient electricity generation, as well as urea removal was also evaluated through DUFC applications.

2. Experimental section

2.1. Preparation of Mxene (MX)

To prepare the Mxene, typically, 1.0 g of Ti_3AlC_2 (MAX phase) was dispersed into a mixture of hydrochloric acid (HCl, 6 M, 20 mL) and lithium fluoride (LiF, 1.5 g) and magnetically stirred at 35 °C for 18 h. The obtained product was recovered through centrifugation and thoroughly rinsed with deionized (DI) water until washing attained a pH = 6.At last, the Ti_3C_2Tx cake was dispersed in DI water under ultrasonic treatment and the clear supernatant was collected after centrifugation for 30 min at 3000 rpm to obtain Ti_3C_2Tx [18,19].

2.2. Preparation of $NiMoO_4$@MX and NiO@MX

Freshly prepared 2 mM of sodium molybdate ($NaMoO_4$) and 2 mM of nickel (II) nitrate hexahydrate ($NiNO_3.6H_2O$) were added into homogeneously dispersed 30 mL of MXene (1 mg/mL) solution. Then 0.5 mM urea was added into the above mixed solution with continued agitation. The resulting mixture was poured into 50 mL Teflon-lined stainless-steel autoclave and hydrothermally treated for 160 °C for 18 h. Subsequently, the precipitate was collected *via* centrifugation, washed with ethanol/water, and dried in a vacuum oven at 80 °C. The final product $NiMoO_4$@MXene ($NiMoO_4$@MX_1) was obtained by calcination at 400 °C for 1 h. Following the same decribed experimental methodolgy, $NiMoO_4$@$MX_{0.5}$ and $NiMoO_4$@$MX_{1.5}$ composites were prepared by using 0.5 mg/mL and 1.5 mg/mL of $Ti_3C_2T_x$ solutions, respectively. Furthermore, NiO@MX_1 and bare $NiMoO_4$ was prepared in the absence of sodium molybdate and MX_1 in the aforementioned experimental parameters.

2.3. Fabrication of freestanding MX and $NiMoO_4$@MX films

MXene, NiO@MX_1, and $NiMoO_4$@$MX_{0.5–1.5}$ were ultrasonically dispersed in DI water (1 mg/mL), and the respective suspensions were vacuum filtered onto a Celgard 3501 membrane. Finally, the resultant freestanding films were dried in air, peeled off from the membrane and stored in an inert atmospheric chamber.

2.4. Physical measurements

The morphology, crystal structure, and elemental composition of prepared materials were investigated by scanning electron microscopy (SEM, JSM5410LV), transmission electron microscopy (TEM), X-ray diffractometer (XRD, Rigaku MiniFlex-600) and X-ray photoelectron spectroscopy (XPS, ESCALAB 250). For TEM analysis, the prepared films were grinded into fine powders and ultrasonically dispersed in ethanol and the required volume of dispersed material was coated over Cu grid.

2.5. Electrochemical measurements

The electrochemical measurements of UOR were performed using CHI650D electrochemical analyzer under ambient condtions. MX or MX composite films (NiO@MX_1 and $NiMoO_4$@$MX_{0.5–1.5}$) assembled in a PTFE replaceable electrode holder served as working electrode, while Pt wire and Hg/HgO were employedas counter and reference electrodes, respectively. UOR was conducted in 0.1 M KOH solution in the presence of urea or human urine or cow urine with optimal concentrations. Urine samples collected from healthy human volunteer and cow were kept for 3 h and centrifuged to remove insoluble impurities. Thereafter,the treated urine samples with pH of 8 ± 1,used as fuel for electrochemical and fuel cell studies. As detailed in our previous research work [20], the reversed-phase high performance liquid chromatography (RP-HPLC) (FL2200) was used to identify the urea concentration in urine samples. With aid of RP-HPLC, urine samples with desired concentration of urea (10–70 mM) were prepared by diluting fresh urine with deionized water. The Hg/HgO reference electrode potential was converted into reversible hydrogen electrode (RHE) using the Nernst equation ($E_{RHE} = E_{(Hg/HgO)} + 0.059*pH + 0.098$) [21,22].

2.6. Fuel cell measurements

DUFC measurement was investigated under single cell setup (**Fig. S1**), consisting of membrane electrode assembly (MEA) sandwiched anode and cathode chamber [20]. The metal nanostructures modified MX films and Pt/C-coated CC were served as anode and cathode, respectively. The MEA was fabricated by sandwiching the AMI-7001 anion exchange membrane (AEM) between the anode and cathode using the glue method. Initially, the anion exchange ionomer sprayed on the AEM surface and the anode is placed over the ionomer sprayed side. After 30 min, anion exchange ionomer was coated on the otherside of AEM and cathode was laminated. Finally, the MEA was left to dried in a vacuum oven at 80 °C for the removal of solvent and air bubbles in the electrode-membrane interface. During the DUFC operation, 70 mM

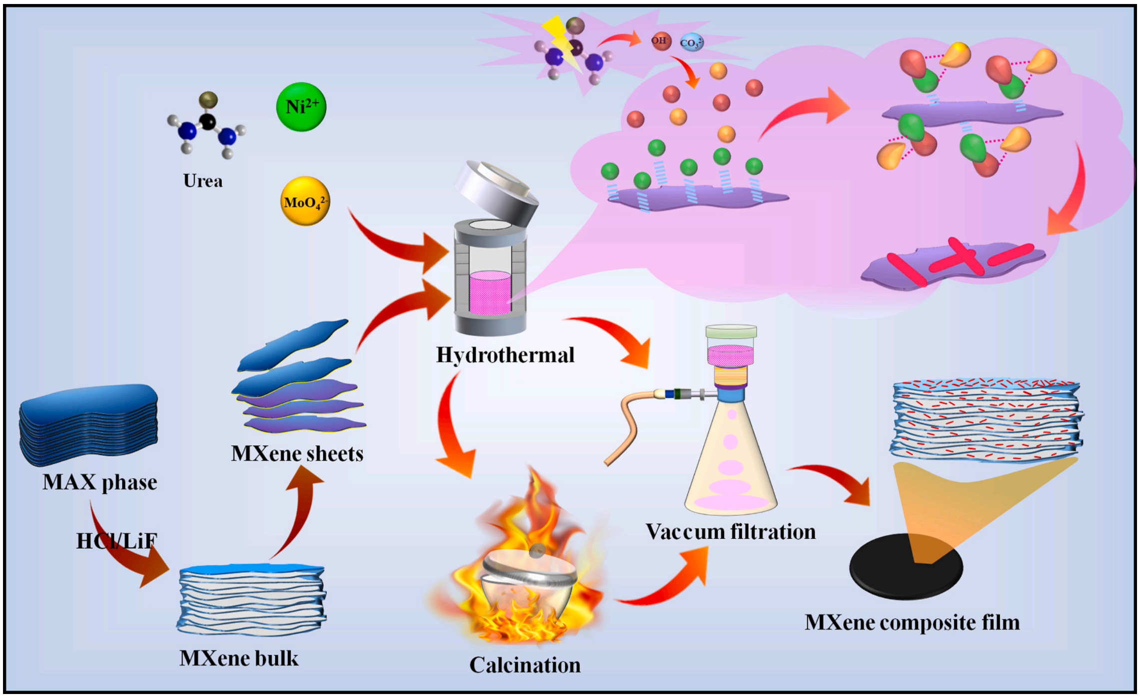

Fig. 1. *Schematic illustration of the* $NiMoO_4$@MX *preparation*. The $NiMoO_4$ is getting decorated in the form of nanoparticles around the MXene sheets.

urea/human urine/cow urine in 0.1 M KOH was injected into the anode chamber (10 mL min^{-1}) and humidified air was supplied into the cathode chamber (200 mL min^{-1}) as the oxidant. To avoid CO_2 poisoning and K_2CO_3 formation, 0.1 M KOH solution used as electrolyte and it was circulated using a peristaltic pump at a flow rate of 10 mL min^{-1}. After stable OCV obtained, the polarization (*I-V*) plots were collected by calculating the cell voltage at room temperature. All DUFC experiments were conducted in triplicate and their average values are reported in the polarization curve.

2.7. Computational method

We conducted density functional theory (DFT) calculations focusing on spin polarization within periodic super-cells. These calculations were based on the generalized gradient approximation (GGA) and employed the Perdew-Burke-Ernzerhof (PBE) functional for exchange-correlation. To represent both nuclei and core electrons, ultrasoft pseudopotentials were utilized. The computational approach involved expanding Kohn-Sham orbitals using a plane-wave basis, with a kinetic energy cutoff of 30 Ry for orbitals and 300 Ry for charge density. Fermi-surface effects were addressed using the Methfessel-Paxton smearing method, with a smearing parameter set to 0.02 Ry. Structural optimization was allowed relaxation of the top half of the atoms until the Cartesian force on each atom reached levels below 10^{-3} Ry/Bohr, and total energy converged within 10^{-5} Ry. For various surfaces like Ti_3C_2-edge, Ti_3C_2-terrace, and $NiMoO_4$(001), Brillouin zone sampling was conducted using k-point meshes of 1 × 2 × 1, 2 × 2 × 1, and gamma. These calculations were executed using the PWSCF codes from the Quantum ESPRESSO package.

3. Results and discussion

3.1. Morphological and structural analysis

Fig. 1 schematically depicts the preparation of freestanding $NiMoO_4$@MX film, including steps of MAX phase etching, hydrothermal treatment, calcination, and vacuum filtration. **Fig. S2** showed the SEM pictures of Ti_3AlC_2 (MX) at different magnification, indicating its smooth surface and irregular grain-like morphology with the particle

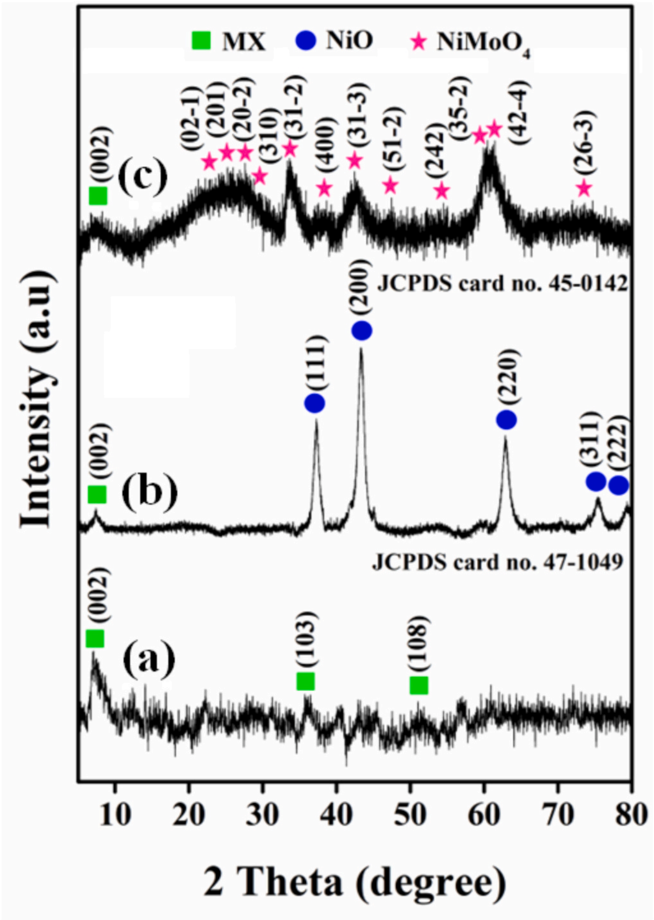

Fig. 2. XRD patterns of (a) MX, (b) NiO@MX_1, and (c) $NiMoO_4$@MX_1.

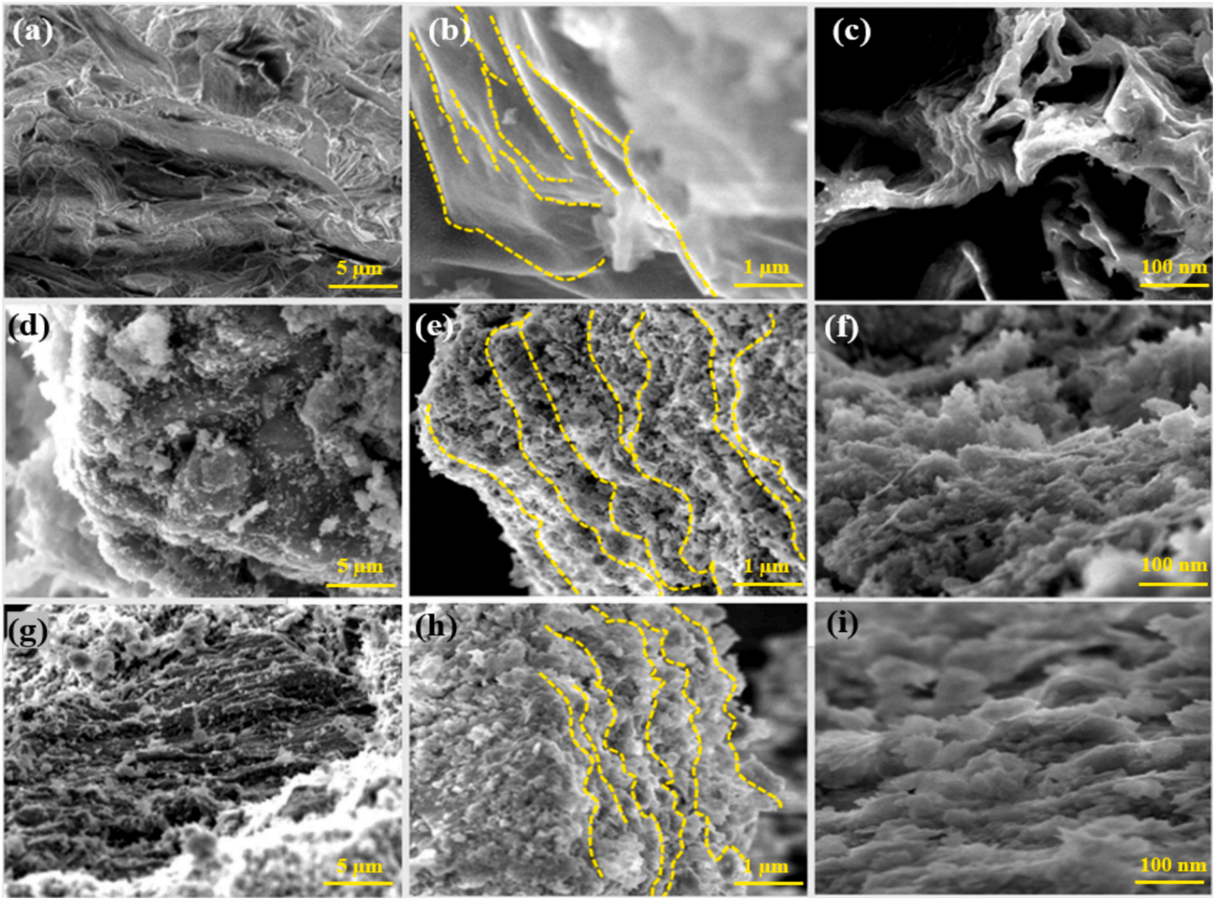

Fig. 3. SEM images *of (a-c) MX, (d-f) NiO@MX_1, and (g-i) $NiMoO_4$@MX_1.* The closed packed, intertwined, coarse like $NiMoO_4$ nanoparticles are decorated over MX sheet. The $NiMoO_4$ is being decorated in the form of nanoparticles around the MXene sheets, highly packed, interconnected, and granular-like $NiMoO_4$ nanoparticles.

size of 2–5 μm.

To characterize the structural features, phase purity, and crystalinity of the prepared samples, XRD technique was employed. Fig. S3a showed the XRD pattern of pristine MAX phase showed the strong signals at 21.31°, 33.64°, 36.72°, 38.71°, 41.48°, 44.76°, 48.19°, 56.24°, 60.7°, 65.45°, 70.27°, and 73.8°, which can be ascribed to the (004), (100), (103), (008), (105), (106), (107), (109), (110), (1011), (1012), and (118) crystal planes, respectively (JCPDS no. 52–0875) [23]. The trivial peaks existed in 21.4°, 29.72°, 31.0°, 40.88°, 42.34° and 77.92° are attributed to the surface oxide impurities of Al in the MAX phase (JCPDS no. 31–0026 and 11–0517) [24]. After acid etching, the peaks centred at 38.69° and 41.57° corresponding to Al are disappeared, along with intensity decreasing of other peaks. Furthermore, the (002) crystal plan peak is broadened and shifted to smaller angle, revealing the selective etching of Al in the MAX phase to form layer structured MX (Fig. 2a) [25]. The etching of Al is further confirmed by the change in morphology, that the bulky grains become wrinkled and stacked sheets with submicron voids between the interconnected sheets (Fig. 3a-c). Subsequent hydrothermal treatment of MX with Ni^{2+} or Ni^{2+}/MoO_4^{2-} amends the MX surface into rough surface and densely grown nanoparticles (Fig. 3d-i). High-resolution SEM images of NiO@MX_1 film showed that the surface and interlayers of MX sheets are uniformly decorated with NiO nanoparticles with a size of about 178 nm (Fig. 3e-f). In this juncture, the formation of NiO is confirmed through the diffraction peaks at 37.4° (111), 43.28° (200), 62.9° (220), 75.29° (311), and 79.2° (222), which are well accordance with cubic NiO (JCPDS no.47–1049) (Fig. 2b) [26].

Under hydrothermal condition, urea is hydrolysed into NH_3 and CO_2, which are further hydrolysed to CO_3^{2-} and OH^- ions, respectively. The generated OH^- ions interact with Ni^{2+} to form $Ni(OH)_x$. XRD profile confirmed the formation of $Ni(OH)_2$, which indicated the existence of hexagonal α-$Ni(OH)_2$ (JCPDS No.22–0444) (Fig. S3b) [20]. Finally, the succeeding calcination process transformed the $Ni(OH)_2$ into NiO. On the other side, when sodium molybdate is introduced into the hydrothermal bath, the generated $Ni(OH)_x$ on MX will react with MoO_4^{2-} to yield $NiMoO_4.xH_2O$@MX [27]. During the hydrothermal reaction, the Ni^{2+} ions will first interact with the negatively charged surface of MX *via* electrostatic interaction. Then, the extended reaction time leads to the formation of $Ni(OH)_x$ and the reaction between $Ni(OH)_x$ and MoO_4^{2-} results in the *in-situ* fabrication of $NiMoO_4.xH_2O$ on MX. The diffraction peaks at 10.85°, 36.57°, 37.51°, 42.92°, 47.68°, 61.83°, 62.61°, and 74.2° are well matched with the standard JCPDS. No 13–0128, confirming the formation of $NiMoO_4.xH_2O$ (Fig. S3c) [28]. Then, $NiMoO_4$@MX_1 is formed by the calcination of $NiMoO_4.xH_2O$@MX_1, due to the removal of water molecules. The removal of water molecules and the conversion of $NiMoO_4.xH_2O$ into $NiMoO_4$ were identified through the XRD peaks at 23° (02−1), 25.37° (201), 27.69° (20−2), 29.32° (310), 33.54° (31−2), 37° (400), 42.76° (31−3), 47.48° (51–2), 54.42° (242), 60.° (35–2), 61.24° (42–4), and 73.42° (26–3), which are synchronized with monoclinic $NiMoO_4$ structure (JCPDS no. 45–0142) (Fig. 2c) [29]. SEM images of $NiMoO_4$@MX_1 show that the MX sheets are decorated with highly packed, interconnected, and granular-like $NiMoO_4$ nanoparticles with a size of 198 nm (Fig. 3g-i). The accompanying EDX elemental mapping shows homogeneous distributions of Ti, C, Ni, Mo, and O elements, signifying the uniform mixture of $NiMoO_4$ and MX (**Fig. S4**).

To further investigate the morphological features, the as-prepared materials were characterized by TEM and high-resolution TEM

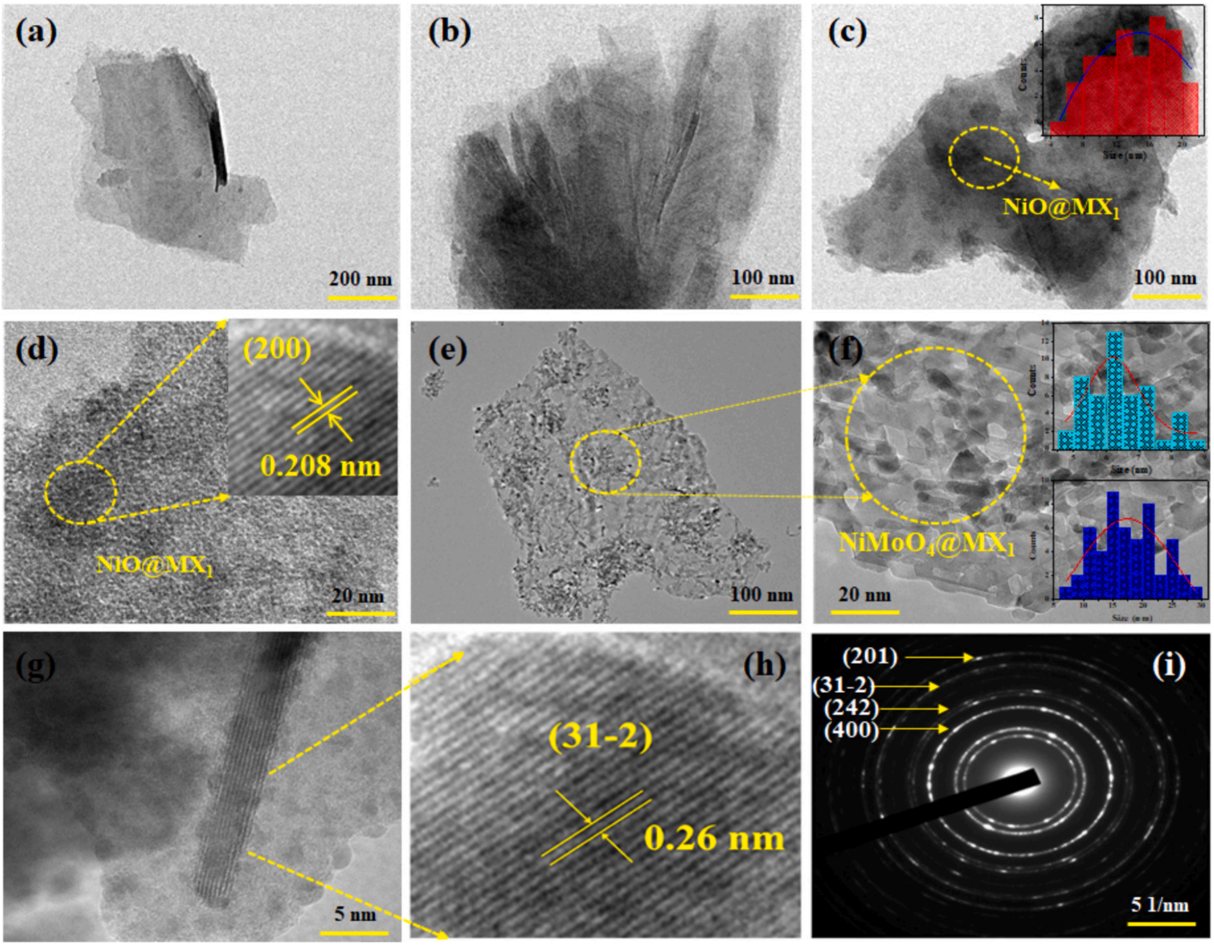

Fig. 4. TEM images of (a,b) MX, (c,d) NiO@MX$_1$, and (e-g) NiMoO$_4$@MX$_1$. (h) HRTEM image and (i) SAED pattern of NiMoO$_4$@MX$_1$. Inset (c) and (f) show statistical data of size distribution of NiO (red), length of NiMoO$_4$ (blue), and width of NiMoO$_4$ (cyan). (For interpretation of the references to colour in this figure legend, the reader is referred to the web version of this article.)

(HRTEM) analyses. As shown in Fig. 4**(a-b)**, MX sheets exhibited well exfoliated, ultrathin, folded, and transparent sheet-like morphology. The size of the MX sheet is observed about 510 ± 60 nm. The TEM images of NiO@MX$_1$ confirmed the NiO nanoparticles are nearly uniformly distributed over the transparent MX sheets (Fig. 4(c-d)). The size of NiO is observed to be 13 ± 4.7 nm (inset Fig. 4(c)). The inset in Fig. 4d denotes the HRTEM image of NiO, exhibiting lattice spacing value of 0.208 nm, ascribing to the (200) plane of NiO. In the case of NiMoO$_4$@MX$_1$, uniformly distributed and smooth surfaced nanorods anchored transparent sheets are observed **(**Fig. 4e-g**)**. The mean length and width of NiMoO$_4$ nanorods are exhibited as 17 ± 5.2 and 6 ± 1.5 nm, respectively **(**inset Fig. 4**f)**. The HRTEM image speculates that the NiMoO$_4$ nanorods are composed of interconnected sphere nanoparticles. Furthermore, a lattice spacing of 0.26 nm was ascribed to the (31–2) plane of NiMoO$_4$ **(**Fig. 4h**)**, and corresponding SAED pattern revealed the polycrystalline nature of NiMoO$_4$ **(**Fig. 4i**)**.

The chemical composition and surface electronic states of fabricated NiMoO$_4$@MX$_1$ material using X-ray photoelectron spectroscopy are shown in Fig. 5. The full scan spectra exhibits all signals of Ti, C, Ni, Mo, and O with respective binding energies (Fig. 5a) [30,31]. The deconvolution of Ni 2p spectrum produces two predominant peaks at 855.7 and 873.2 eV along with their satellite peaks at 861.5 eV and 879.6 eV, respectively. These deconvoluted peaks are ascribed to the Ni 2p$^{3/2}$ and Ni 2p$^{1/2}$ orbital peaks, confirming the existence of Ni^{2+} oxidation state in the NiMoO$_4$ (Fig. 5b) [32]. Furthermore, the Mo 3d XPS spectra show two peaks at 232.2 eV and 235.3 eV, ascribing to the Mo 3d$^{5/2}$ and Mo 3d$^{3/2}$ orbital peaks, respectively (Fig. 5c) [31], revealing the existence of molybdenum in Mo^{6+} oxidation state in the NiMoO$_4$. The Ti 2p spectrum can be deconvoluted into four peaks at 454.6, 456.2, 459.1, and 460.8 eV, which are corresponding to Ti—C (Ti 2p$_{3/2}$), Ti—O (Ti 2p$_{3/2}$), Ti—C (Ti 2p$_{1/2}$), and Ti—O (Ti 2p$_{1/2}$) bonds, respectively (Fig. 5d) [33]. Furthermore, the C1s spectrum can be deconvoluted to four peaks at 282.8, 284.5, 285.8, and 288.8 eV, attributing to C—Ti, C—C, C—O, and C—F bonds, respectively (Fig. 5e) [34]. The signals of O 1s at 530.3 and 531.3 eV are typical characteristics of the adsorbed and lattice oxygen, respectively (Fig. 5f) [32,33].

3.2. *Electrochemical studies*

The electrochemical performance of fabricated MX films is evaluated in a three-electrode system with 0.1 M KOH electrolyte (Fig. 6a). As can be observed, the cyclic voltammetry (CV) curve of bare MX exhibits no redox peaks, while the NiO@MX$_1$ and NiMoO$_4$@MX$_1$ show a well-defined redox couple in the potential range of 1.0–1.624 V (*vs.* RHE). As detailed in Fig. 6d, the redox peaks are attributed to the reaction of Ni^{2+}/Ni^{3+} in NiO@MX$_1$, while the reactions of Ni^{2+}/Ni^{3+} and Mo^{3+}/Mo^{4+} in NiMoO$_4$@MX$_1$ [20,35,36]. Owing to the variable transition metal oxidation states and high electrical conductivity, the NiMoO$_4$@MX$_1$ exhibits higher redox peak current than NiO@MX$_1$. To Figure out the kinetics of NiMoO$_4$@MX$_1$ redox reactions, CVs are recorded at different scan rates in the rage of 10–100 mV s^{-1}. The derived square root of the scan rate *versus* current ($v^{1/2}$ *vs.* I$_p$) plot shows that the anodic (I$_{pa}$) and cathodic (I$_{pc}$) peak current linearly increased with scan rate. The results of $v^{1/2}$ *vs.* I$_p$ plot and the high correlation

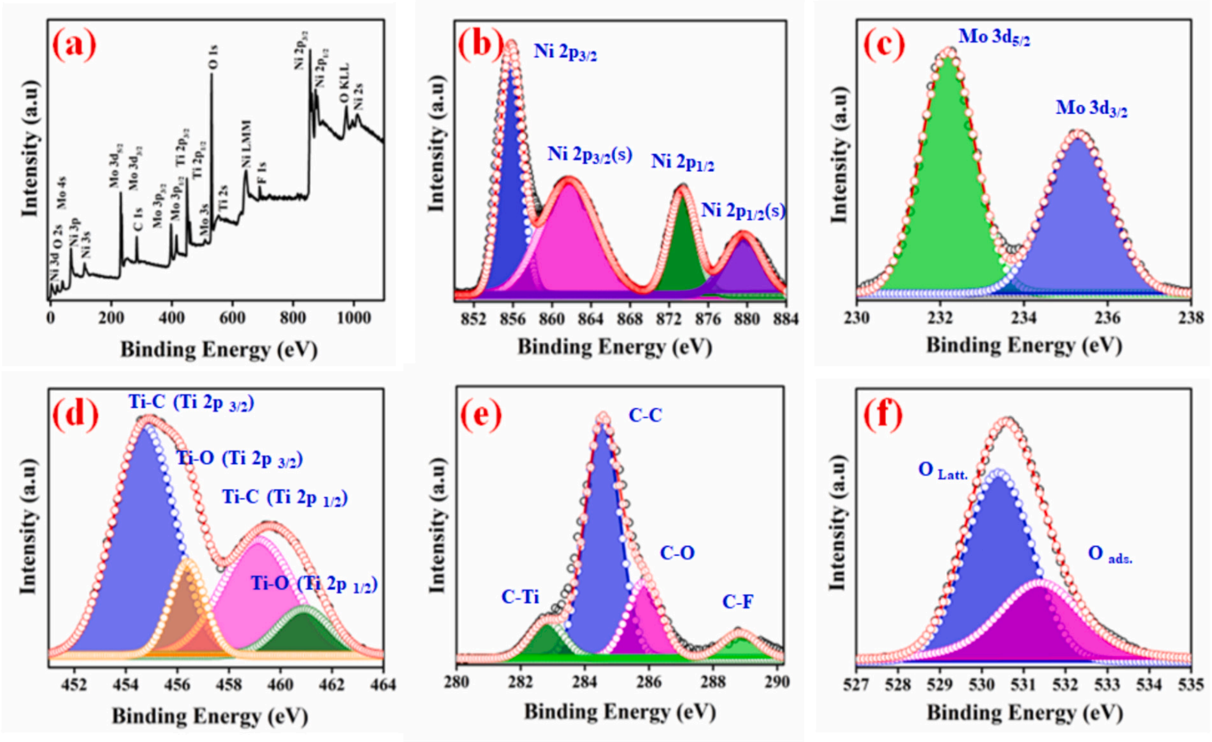

Fig. 5. XPS (a) survey spectra, (b) Ni 2p, (c) Mo 3d, (d) Ti 2p, (e) C 1s, and (f) O 1s spectra of $NiMoO_4@MX_1$.

coefficients (R) of I_{pa} (0.990) and I_{pc} (0.989) reveal the association of diffusion-controlled processes in $NiMoO_4@MX_1$ (**Fig. S5**).

The performance of UOR on MX, $NiO@MX_1$ and $NiMoO_4@MX_1$ films are conducted in 0.1 M KOH solution with the presence of urea (Fig. 6b). The bare MX shows no response of UOR due to its inactive behavior and absence of active metal redox couples. In contrast, the $NiO@MX_1$ can generate Ni^{2+}/Ni^{3+} redox couple as active sites to oxidize urea, as evidenced by the increased I_{pa} of 17.12 mA/cm^2 at E_{pa} of 1.512 V (*vs.* RHE). The $NiMoO_4@MX_1$ showed improved UOR behavior, which achieved higher I_{pa} of 49.70 mA at 1.479 V (*vs.* RHE). An onset potential is a vital parameter for assessing electrocatalytic property of prepared materials and has been calculated at 10 mA cm^{-2}. The $NiMoO_4@MX_1$ exhibits oxygen evolution reaction (OER) potential of 1.434 V (*vs.* RHE) at 10 mA cm^{-2} and it has been decreased to 1.355 V after the addition of 70 mM urea because of urea oxidation reaction (UOR). The obtained 1.355 V at 10 mA cm^{-2} is denoted as UOR potential and the UOR potential of MX, $NiO@MX_1$, $NiMoO_4@MX_1$ in the order of 1.616 V > 1.454 V > and 1.355 V, respectively. The potential difference between MX and $NiMoO_4@MX_1$ is exhibited about 261 mV, demonstrating the better efficiency of $NiMoO_4@MX_1$ toward better UOR activity. To verify the applicability of $NiMoO_4@MX_1$ toward real samples, UOR was studied using human urine and cow urine (added in 0.1 M KOH) as the electrolyte. Surprisingly, the electrochemical responses of human urine and cow urine are similar with the urea solution, and there are only negligible UOR potential deviations (Fig. 6c). The UOR potentials of human urine (1.381 V, *vs.* RHE) and cow urine (1.362 V, *vs.* RHE) at 10 mA cm^{-2} are slightly higher than that in urea, possibly due to the existence of complex species in urine samples.

Fig. 6d details the catalytic mechanism. In specific, the Ni^{2+} and Mo^{3+} of $NiMoO_4$ are converted into Ni^{3+} and Mo^{4+} under alkaline condition, respectively [36]. Then, the generated Ni^{3+} and Mo^{4+} react with urea to produce electrons (e^-), N_2, CO_2, and H_2O, while they are reduced back to Ni^{2+} and Mo^{3+} for the next cycle. The one-dimensional (1D) rod-like morphology of $NiMoO_4$ and its intact contact with MX facilitate the continuous formation of Ni^{2+}/Ni^{3+} and Mo^{3+}/Mo^{4+} redox couples and enhance the electron transportation at the electrode-electrolyte interface, thereby improving the UOR activity of $NiMoO_4@MX_1$. The composition of $NiMoO_4$ and MX are optimized, that the CVs of $NiMoO_4@MX_{(0.5–1.5)}$ series showed that the $NiMoO_4@MX_1$ is the most efficient for UOR (**Fig. S6**). Accordingly, $NiMoO_4@MX_1$ is selected for entire electrochemical and fuel cell studies.

The UOR responses of $NiMoO_4@MX_1$ with different concentrations of the urea and different volumes of human/cow urine are presented in Fig. 7. The I_{pa} in the CVs increases as the increase of urea concentration (Fig. 7a), human urine (HU) (Fig. 7b), and cow urine (CU) (Fig. 7c) volume, inferring the robust structural rigidity of $NiMoO_4@MX_1$ against the surface fouling reaction. Furthermore, CV curves under different scan rates ranging from 10 to 100 mV s^{-1} with the electrolyte of 0.1 M KOH containing urea (Fig. 7d), human urine (Fig. 7e) and cow urine (Fig. 7f) are acquired. It is observed that the plots of I_{pa} *vs.* $v^{1/2}$ plots has good linear relationship with high correlation coefficients (R) of 0.998 (urea), 0.998 (human urine), and 0.997 (animal urine), revealing the contribution of diffusion-controlled process in $NiMoO_4@MX_1$ during UOR (**Fig. S7**).

To further probe the stability of $NiMoO_4@MX_1$ during UOR, amperometry i–t studies are performed at an applied potential of 1.45 V (*vs.* RHE) (**Fig. S8**). The strong structural integrity and robustness of fabricated $NiMoO_4@MX_1$ facilitates the generation of constant current throughout the reaction under the presence of urea, human urine and cow urine. The firm structural integrity is further confirmed from the increasing current response with increasing urea concentration from 10 mM to 70 mM in amperometry analysis **(Fig. S9)**. Similar with CV results, the current response of $NiMoO_4@MX_1$ in urea solution is higher than those in human urine and cow urine. The slight current fluctuation experienced with increasing time is attributed to the perturbation of gas molecules over the electrode surface. However, as per previously reported results, the presence of complex interference species in human urine may be responsible for the current fluctuation [37]. In order to verify the influences of interference species, interference study is performed at an applied potential of 1.45 V (*vs.* RHE) with addition of different interference species (**Fig. S10**). Based on the composition of human urine and cow urine, the interference species are selected and

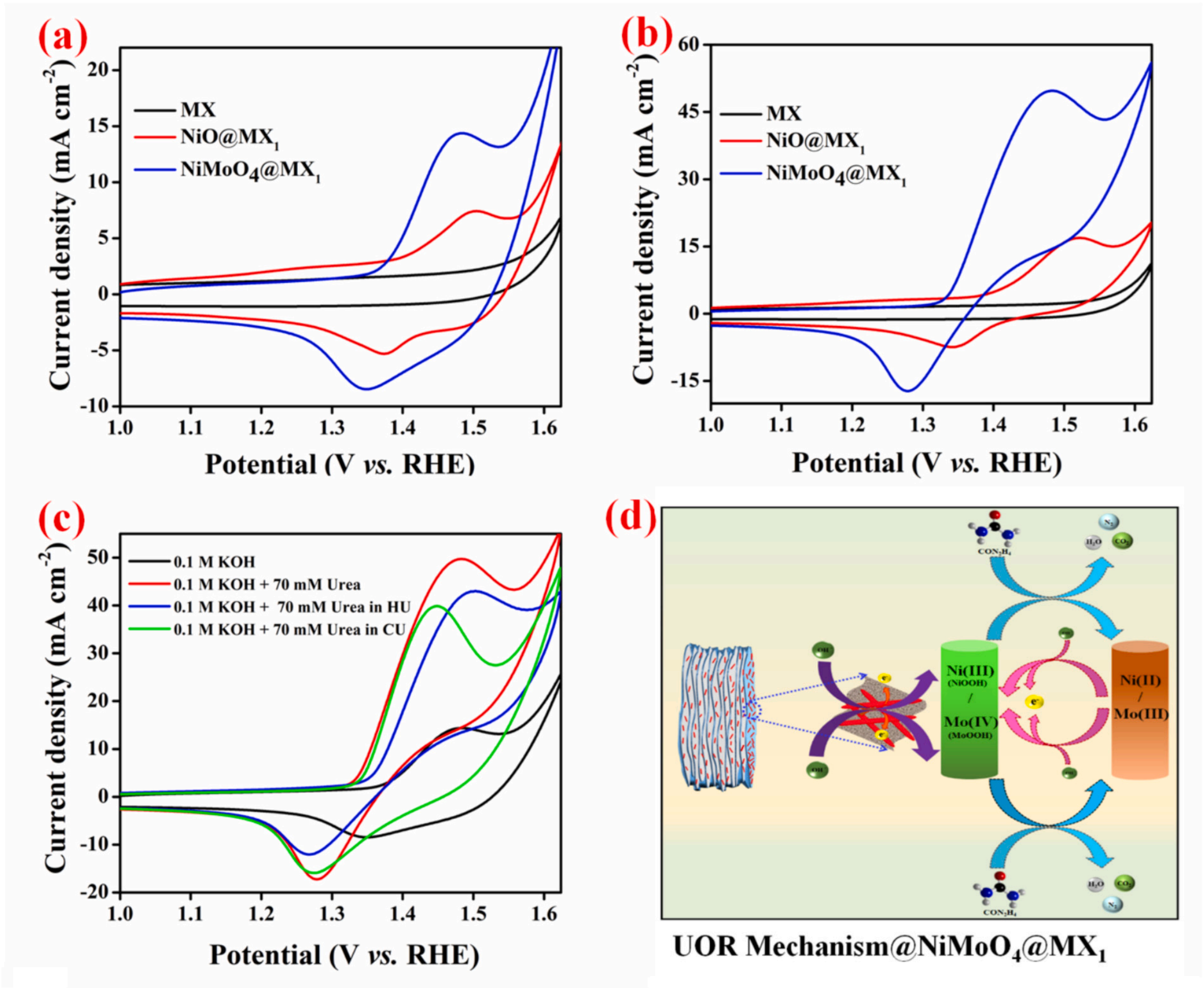

Fig. 6. (a) CVs of the MX electrodes in 0.1 M KOH, and (b) CVs of the MX electrodes in 50 mM urea added 0.1 M KOH at a scan rate of 50 mV s^{-1}, *(c)* CVs of NiMoO$_4$@MX$_1$ in urea, human urine (HU) and cow urine (CU) added 0.1 M KOH, (d) the UOR mechanism involved at NiMoO$_4$@MX$_1$.

separately added into the solution at different time intervals [38,39]. Except for glucose solution, the other interference species do not alter the current responses of NiMoO$_4$@MX$_1$. Although glucose increases trivial current responses, the produced current seems stable; thereby the NiMoO$_4$@MX$_1$ is highly stable against interference species. Hence, it is confirmed that the generation of gas molecules during UOR is only responsible for trivial current fluctuation in the amperometry results.

Further, the density functional theory (DFT) analysis was conducted to gain the atomic understanding of NiMoO$_4$@MX$_1$. In order to realize the interaction between NiMoO$_4$ and Ti$_3$C$_2$ in the NiMoO$_4$@MX$_1$ heterostructure, we calculated the charge density difference and density of states (DOS). **Fig. S11a** shows the relaxed-created slab of NiMoO$_4$@MX$_1$ heterostructure along with crystal parameters. The charge density difference profile **(Fig. S11b)** clearly indicated the significant electron density exchange between NiMoO$_4$ and Ti$_3$C$_2$, confirming the electronic interaction between both NiMoO$_4$ and Ti$_3$C$_2$ in the NiMoO$_4$@MX$_1$ heterostructure. Furthermore, the improved density of states over the fermi-level in the case of the NiMoO$_4$@MX$_1$ heterostructure demonstrated the significant enhancement in electronic conductivity of NiMoO$_4$@MX$_1$ due to heterojunction interaction **(Fig. S11c)**, which benefited its electrochemical performances. Further, computational hydrogen electrode (CHE) method [40] was introduced to discuss the activity and the reaction Free energy diagrams (FED) for UOR was plotted in Fig. 8. The three associated surfaces are plotted by Ti$_3$C$_2$ edge (red), Ti$_3$C$_2$-terrace (black) and NiMoO$_4$ (blue). The "virtual energetic span" (δE^v) is introduced as the activity determining term [41]. From the descriptor, it is concluded that (1) it can connect with the TOF by TOF = $k_0\exp(-\delta E^v/RT)$, where k_0 - the standard reaction kinetic constant; (2) δE^v can be calculated by the difference between virtual TOF determining transition state (TDTS^v) and the TOF determining intermediates (TDI), *i.e.*, δE^v = TDTS^v- TDI. In each FED in Fig. 8**(a,b)**, the positions of the TDTS^v and TDI are connected with an arrow, pointing from TDI to TDTS^v.

In the case of UOR, for single phases, the activity, indicating by the largest Gibbs energy difference among all steps (ΔG^0_{max}), is higher on NiMoO$_4$ (δE^v = 1.26 eV) than that of Ti$_3$C$_2$ (δE^v = 4.60 eV and 1.35 eV for terrace and edge sites, respectively). This indicates that the NiMoO$_4$ should be the exact active site, if only comparing the single phase. Moreover, if including the interphase for the composite structure of NiMoO$_4$ and Ti$_3$C$_2$, an additional UOR pathway with higher activity can be inferred. That is, the adsorption of CON$_2$H$_4$ and cracking of C—N bonds are occurred on the Ti$_3$C$_2$ first, then shift to the NiMoO$_4$ to complete the left steps. This step will have the smallest δE^v of 0.41 eV, which is represented in yellow dashed line, indicating the benefits of hybrid phases of NiMoO$_4$@Ti$_3$C$_2$.

3.3. Fuel cell performance analysis

Based on the above UOR investigation, direct urea fuel cells (DUFCs) were assembled by pairing different anodes (including bare MX, NiO@MX$_1$, and NiMoO$_4$@MX$_1$) with Pt/C-coated carbon cloth (Pt/C/CC) cathode, with using 0.1 M KOH containing 70 mM urea as the

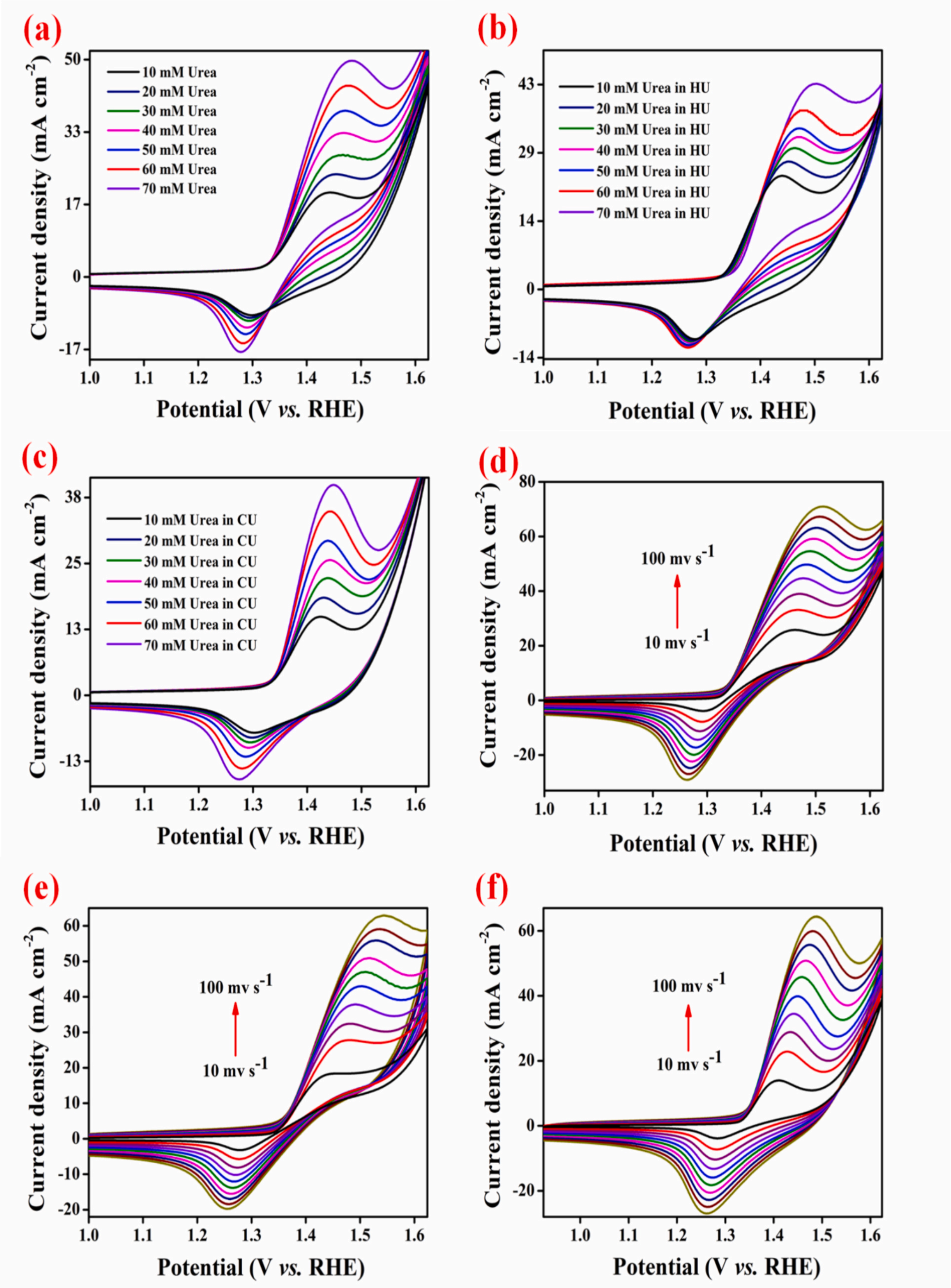

Fig. 7. CVs of NiMoO$_4$@MX$_1$ as a function of (a) urea concentration, (b) urea in human urine, and (c) urea in cow urine (CU) in 0.1 M KOH at a scan rate of 50 mV s^{-1}. CVs of NiMoO$_4$@MX$_1$ in the presence of (d) urea, (e) human urine, and (f) cow urine as a function of scan rate ranging from 10 to 100 mV s^{-1} in 0.1 M KOH.

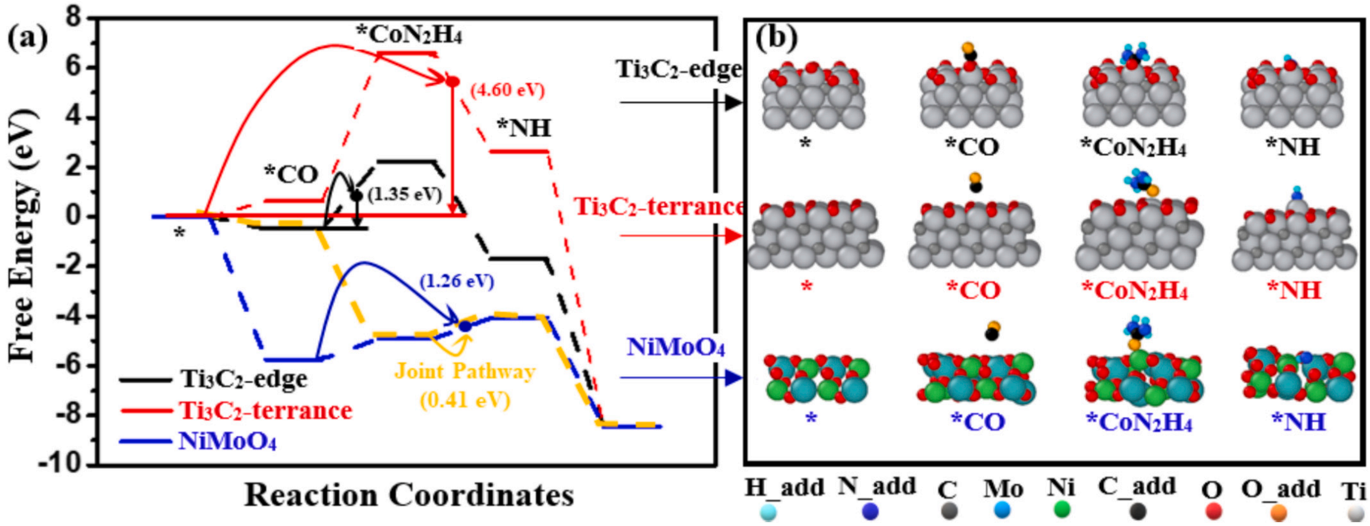

Fig. 8. Reaction free energy diagram of (a) UOR and on $NiMoO_4@Ti_3C_2$ and the associated optimized structures of (b) UOR intermediates. The black, red and blue plots are the FEDs of UOR on Ti_3C_2-edge, Ti_3C_2-terrace and $NiMoO_4$, respectively. The yellow dashed line is correspond to the joint pathway. The arrows in (a) and (c) connect the $TDTS^v$ and TDI of each FED, pointing from TDI to $TDTS^v$. Their differences in energy ($TDTS^v$ - TDI, unit: eV) can be connected with TOF by TOF∝exp.[−($TDTS^v$ - TDI)/RT]. We define $\delta E^v = TDTS^v - TDI$, which is named as "virtual energetic span". (c) and (d) repersents the corresponding mechanisms, respectively. (For interpretation of the references to colour in this figure legend, the reader is referred to the web version of this article.)

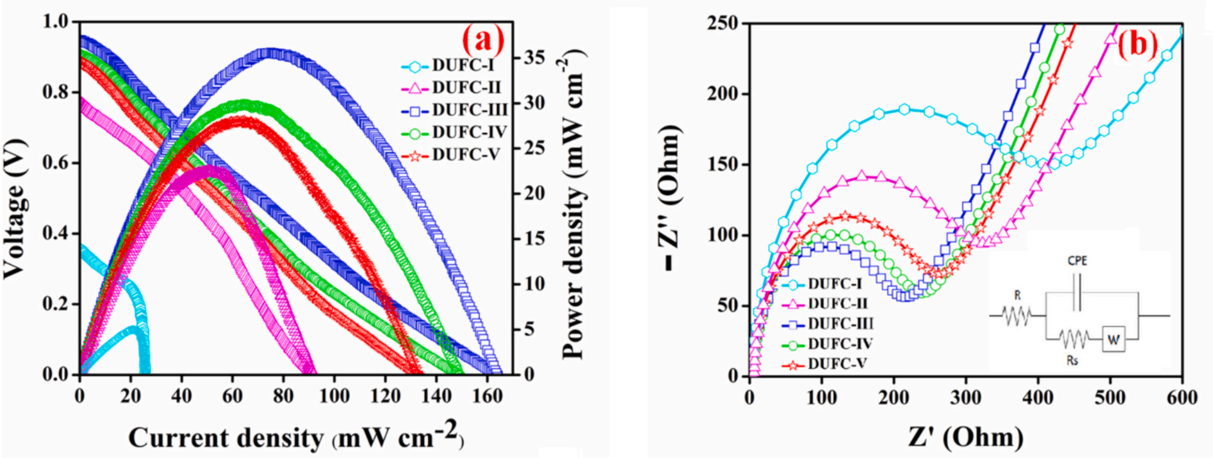

Fig. 9. Polarization plots of (a) DUFCs and their corresponding (b) Nyquist plots of with different anodes. Insets correspond to their respective randles equivalent circuit diagram.

electrolyte. The constructed fuel cells are denoted as DUFC-I (MX‖Pt/C/CC), DUFC-II ($NiO@MX_1$‖Pt/C/CC), and DUFC-III ($NiMoO_4@MX_1$‖Pt/C/CC). As shown in Fig. 9a, the DUFC-III exhibited a maximum power density of 35.4 mW cm^{-2} and a current density of 163 mA cm^{-2}, which are considerably superior than DUFC-I (4.8 mW cm^{-2} / 26 mA cm^{-2}) and DUFC-II (22.5 mW cm^{-2} /89 mA cm^{-2}). The high performance of the DUFC-III can be accredited to the following favourable perceptions of $NiMoO_4@MX_1$. First, the interconnected MX nanosheets possess abundant surface voids, which act as a sturdy reservoir for the accommodation of more analytes. Second, the adsorption of urea molecules over MX and $NiMoO_4$ surface through hydrogen bonds and M–O and O-C bridging coordination bonds, respectively, yielding close analytes contact to the electrode surface [42,43]. Additionally, the continuous generation of bimetallic active sites of Ni^{2+}/Ni^{3+} and Mo^{3+}/Mo^{4+} under alkaline condition contribute to efficient UOR, which produce more electrons to transfer to the cathode *via* external circuit. Thus, the rapid electron transference from anode to cathode supports for larger power performance to DUFC-III.

The electrochemical impedance spectroscopy (EIS) study of DUFCs is performed with 0 to 0.1 kHz frequency range and the derived Nyquist plot is shown in Fig. 9b. Among the studied fuel cells, the minimal charge-transfer resistance (R_{ct}) of 214 Ω is achieved for the DUFC-III, demonstrating the higher electron transference with increasing charge transfer rate. The *in-situ* preparation approach creates an intact contact between $NiMoO_4$ and MX_1, supporting the convenient electron transportation between the active 1D $NiMoO_4$ and the conducting 2D MX support. The interfacial resistance is minimized by the uninterrupted electron flow in $NiMoO_4@MX_1$, therefore resulting in the high performances of the DUFC-III. When feeding with human urine or cow urine (in 0.1 M KOH), the DUFC achieved the power and current densities of 29.8 mW cm^{-2}/132 mA cm^{-2} (Human urine, DUFC-IV) and 27.9 mW cm^{-2}/91 mA cm^{-2} (Cow urine, DUFC-V) (Fig. 9). Although the urine-powered DUFC-IV and DUFC-V devices showed inferior power performances lower than the other DUFCs, the proposed work opens a new path for real applications. Furthermore, the strong structural integrity and synergism of MX and $NiMoO_4$ yields high durability without any obvious performance loss. **Table S1** compared the reported DUFC with other previously reported urea fuel cells operated under similar operating conditions. The removal of urea in analyte solution after the DUFC operation is calculated to be 94 and 92 % respective to the human urine and cow urine fuels, respectively. The obtained outcome actualizes the excellent performance of DUFC-III, owing to the betterment of electrocatalytic acidity of $NiMoO_4@MX_1$ toward UOR. The post-morphological characteristics of $NiMoO_4@MX_1$ after the DUFC operation were performed to further confirm the stability of $NiMoO_4@MX_1$. As shown in **Fig. S12a**, the layered structure of MX is covered by coarse like particles due to the adsorption of urea molecules or oxidation products. However, the decoration of $NiMoO_4$ over MX_1 has not altered as evidenced from their TEM results (**Fig. S12b**).

Recently, artificial intelligence (AI) receives significant attention in the materials design and their optimization toward electrocatalytic applications. When compared with traditional “trial-and-error” method, the utilization of AI techniques provides cost and time efficient materials design strategy. As future perspectives of $NiMoO_4@MX$ toward futuristic energy application, it is expected that the DFT-derived electronic signifiers including charge density distributions, adsorption energies, and density states would act as training datasets for predictive ML models. These ML models can provide a heterostructure combinations screening, optimal UOR surface configuration, and validate the stability of catalysts toward fuel cell conditions. Additionally, coupling AI with real-time fuel equipped electrochemical analysis may offer a development of self-optimizing DUFC, operated with varying fuel configurations such as human and animal wastes fuels. Hence, it is expected that the synergy between experimentation, quantum level DFT insights, and AI/ML-assisted strategy can create a new dimension toward scalable, smart, and ecological urea-to-energy conversion technologies.

4. Conclusions and future perspectives

In summary, freestanding $NiMoO_4@MX$ film is well-engineered as a bifunctional catalyst for electrochemical UOR. Due to the rationally designed structure and the synergistic effects between 2D MX and 1D $NiMoO_4$, the fabricated $NiMoO_4@MX_1$ produces higher DUFC performance over previously reported catalysts materials. Also, the production of 29.8, and 27.9, mW cm^{-2} power densities under human urine, and cow urine unveil the ability of $NiMoO_4@MX_1$ toward real fuel-based sustainable electricity generation. As expected, these outcomes open a new avenue for simultaneous waste management and sustainable electricity generation as ‘two birds-one stone’ strategy.

CRediT authorship contribution statement

Senthilkumar Nangan: Writing – original draft, Methodology, Investigation. **Yogapriya Selvaraj:** Writing – review & editing. **Manunya Okhawilai:** Supervision, Funding acquisition. **Anbazhagan Venkattappan:** Validation, Resources. **Anuj Kumar:** Software. **Mohd Ubaidullah:** Project administration, Formal analysis.

Declaration of competing interest

The authors declare that they have no known competing financial interests or personal relationships that could have appeared to influence the work reported in this paper.

Acknowledgments

This work was supported by the Second Century Fund (C2F), Science Research and Innovation Fund (IND_FF_68_220_6200_009), Chulalongkorn University, Thailand. National Research Council of Thailand (NRCT) and Chulalongkorn University (N42A660910) and the NSRF via the Program Management Unit for Human Resources & Institutional Development, Research and Innovation (B49G680121) are also acknowledged. The authors extend their sincere appreciation to the Ongoing Research Funding program, (ORF-2025-682), King Saud University, Riyadh, Saudi Arabia for the support.

Appendix A. Supplementary data

Supplementary data to this article can be found online at https://doi.org/10.1016/j.microc.2025.115770.

Data availability

Data will be made available on request.

References

[1] Z. Kong, J. Wu, Z. Liu, D. Yan, Z.-P. Wu, C.-J. Zhong, Advanced electrocatalysts for fuel cells: Evolution of active sites and synergistic properties of catalysts and carrier materials, Exploration 5 (2025) 20230052, https://doi.org/10.1002/EXP.20230052.

[2] G. Gnana Kumar, A. Farithkhan, A. Manthiram, Direct urea fuel cells: recent Progress and critical challenges of urea oxidation electrocatalysis, Adv. Energy Sustain. Res. 1 (2020) 2000015, https://doi.org/10.1002/aesr.202000015.

[3] L. Zhang, L. Wang, H. Lin, Y. Liu, J. Ye, Y. Wen, A. Chen, L. Wang, F. Ni, Z. Zhou, S. Sun, Y. Li, B. Zhang, H. Peng, A lattice-oxygen-involved reaction pathway to boost urea oxidation, Angew. Chem. 131 (2019) 16976–16981, https://doi.org/10.1002/ange.201909832.

[4] K. Ye, H. Zhang, L. Zhao, X. Huang, K. Cheng, G. Wang, D. Cao, Facile preparation of three-dimensional Ni(OH)2/Ni foam anode with low cost and its application in a direct urea fuel cell, New J. Chem. 40 (2016) 8673–8680, https://doi.org/10.1039/c6nj01648k.

[5] J. Yoon, D. Lee, Y.N. Lee, Y.S. Yoon, D.J. Kim, Solid solution palladium-nickel bimetallic anode catalysts by co-sputtering for direct urea fuel cells (DUFC), J. Power Sources 431 (2019) 259–264, https://doi.org/10.1016/j.jpowsour.2019.05.059.

[6] X. He, X. Han, X. Zhou, J. Chen, J. Wang, Y. Chen, L. Yu, N. Zhang, J. Li, S. Wang, H. Jin, Electronic modulation with Pt-incorporated NiFe layered double hydroxide for ultrastable overall water splitting at 1000 mA cm−2, Appl. Catal. Environ. 331 (2023) 122683, https://doi.org/10.1016/j.apcatb.2023.122683.

[7] M. Ranjani, N. Senthilkumar, G. Gnana Kumar, A. Manthiram, 3D flower-like hierarchical NiCo2O4 architecture on carbon cloth fibers as an anode catalyst for high-performance, durable direct urea fuel cells, J Mater Chem A 6 (2018) 23019–23027, https://doi.org/10.1039/c8ta08405j.

[8] Y. Zhao, X. Liu, X. Wang, P. Zhang, J. Shi, Peony petal-like 3D graphene-nickel oxide nanocomposite decorated nickel foam as high-performance electrocatalyst for direct glucose alkaline fuel cell, Int. J. Hydrogen Energy 42 (2017) 29863–29873, https://doi.org/10.1016/j.ijhydene.2017.10.120.

[9] R. Paulose, R. Mohan, V. Parihar, Nanostructured nickel oxide and its electrochemical behaviour—a brief review, Nano-Struct. Nano-Objects 11 (2017) 102–111, https://doi.org/10.1016/j.nanoso.2017.07.003.

[10] P. Peng, X.M. Lin, Y. Liu, A.S. Filatov, D. Li, V.R. Stamenkovic, D. Yang, V. B. Prakapenka, A. Lei, E.V. Shevchenko, Binary transition-metal oxide hollow nanoparticles for oxygen evolution reaction, ACS Appl. Mater. Interfaces 10 (2018) 24715–24724, https://doi.org/10.1021/acsami.8b06165.

[11] S. Wang, C. Sun, N. Wang, Q. Zhang, Ni- and/or Mn-based layered transition metal oxides as cathode materials for sodium ion batteries: status, challenges and countermeasures, J Mater Chem A 7 (2019) 10138–10158, https://doi.org/10.1039/c8ta12441h.

[12] M.M. Sk, C.Y. Yue, K. Ghosh, R.K. Jena, Review on advances in porous nanostructured nickel oxides and their composite electrodes for high-performance supercapacitors, J. Power Sources 308 (2016) 121–140, https://doi.org/10.1016/j.jpowsour.2016.01.056.

[13] N. Zhang, X. Xiao, H. Pang, Transition metal (Fe, Co, Ni) fluoride-based materials for electrochemical energy storage, Nanoscale Horizons 4 (2019) 99–116. Doi: https://doi.org/10.1039/c8nh00144h.

[14] M. Yang, Q. Bai, C. Ding, NiMoO4 nanoparticles embedded in nanoporous carbon nanosheets derived from peanut shells: efficient electrocatalysts for urea oxidation, Colloids Surf. A Physicochem. Eng. Asp. 604 (2020), https://doi.org/10.1016/j.colsurfa.2020.125276.

[15] P. Kannan, F. Chen, H. Jiang, H. Wang, R. Wang, P. Subramanian, S. Ji, Hierarchical core-shell structured Ni3S2/NiMoO4 nanowires: a high-performance and reusable electrochemical sensor for glucose detection, Analyst 144 (2019) 4925–4934, https://doi.org/10.1039/c9an00917e.

[16] J. Kundu, T. Kwon, K. Lee, S.-I. Choi, Exploration of metal-free D electrocatalysts toward the oxygen Electroreduction, Exploration 4 (2024) 20220174, https://doi.org/10.1002/EXP.20220174.

[17] P. Liu, Z.H. Zhu, W. Zhang, J.Y. Liu, Z. Su, X.H. Liu, S.C. Yang, C. Lai, Shearing-force-driven delamination of waste residue into oxidatively stable MXene composites for high-performance Si anode, Rare Metals 42 (2023) 2226–2237, https://doi.org/10.1007/s12598-022-02182-z.

[18] A. Lipatov, M. Alhabeb, M.R. Lukatskaya, A. Boson, Y. Gogotsi, A. Sinitskii, Effect of synthesis on quality, electronic properties and environmental stability of individual monolayer Ti3C2 MXene flakes, Adv. Electronic Mater. 2 (2016), https://doi.org/10.1002/aelm.201600255.

[19] Y. Wang, J. Sun, X. Qian, Y. Zhang, L. Yu, R. Niu, H. Zhao, J. Zhu, 2D/2D heterostructures of nickel molybdate and MXene with strong coupled synergistic effect towards enhanced supercapacitor performance, J. Power Sources 414 (2019) 540–546, https://doi.org/10.1016/j.jpowsour.2019.01.036.

[20] N. Senthilkumar, G. Gnana kumar, A. Manthiram, 3D Hierarchical Core–Shell Nanostructured Arrays on Carbon Fibers as Catalysts for Direct Urea Fuel Cells, Adv. Energy Mater. 8 (2018) 1–11. Doi: https://doi.org/10.1002/aenm.201702207.

[21] S. Nangan, M. Okhawilai, P. Senthil Kumar, D. Verma, K. Rajendran, J. Qin, H. Uyama, Baby diaper's super absorbent polymer derived carbon templated NiCuP@NiCu nanostructures for green hydrogen production, Int. J. Hydrogen Energy (2023), https://doi.org/10.1016/j.ijhydene.2023.02.069.

[22] S. Nangan, T. Natesan, W. Sukmas, M. Okhawilai, K. Justice Babu, P. Tsuppayakorn-aek, T. Bovornratanaraks, T. Wongsalam, V. Vimal, H. Uyama, A. M. Al-Enizi, L. Kansal, S.S. Sehgal, Waste plastics derived nickel-palladium alloy filled carbon nanotubes for hydrogen evolution reaction, Chemosphere 341 (2023) 139982, https://doi.org/10.1016/j.chemosphere.2023.139982.

[23] J. Xu, X. Yang, Y. Zou, L. Zhu, F. Xu, L. Sun, C. Xiang, J. Zhang, High density anchoring of NiMoS4 on ultrathin Ti3C2 MXene assisted by dopamine for supercapacitor electrode materials, J. Alloys Compd. 891 (2022) 161945, https://doi.org/10.1016/j.jallcom.2021.161945.

[24] B. Scheibe, V. Kupka, B. Peplińska, M. Jarek, K. Tadyszak, The Influence of Oxygen Concentration during MAX Phases (Ti 3 AlC 2) Preparation on the αAl 2 O 3 Microparticles Content and Specific Surface Area of Multilayered MXenes (Ti 3 C 2 T x), Materials 12 (2019) 1–11. Doi: https://doi.org/10.3390/ma12030353.

[25] J. Li, X. Yuan, C. Lin, Y. Yang, L. Xu, X. Du, J. Xie, J. Lin, J. Sun, Achieving high Pseudocapacitance of 2D titanium carbide (MXene) by cation intercalation and surface modification, Adv. Energy Mater. 7 (2017), https://doi.org/10.1002/aenm.201602725.

[26] U.T. Nakate, P. Patil, S.P. Choudhury, S.N. Kale, Microwave assisted synthesis of Co3O4 and NiO nanoplates and structural, optical, magnetic characterizations, Nano-Struct. Nano-Objects 14 (2018) 66–72, https://doi.org/10.1016/j.nanoso.2018.01.007.

[27] A.S. Keshari, P. Dubey, Rapid microwave-assisted vs. hydrothermal synthesis of hierarchical sheet-like NiO/NiMoO4 hybrid nanostructures for high performance extrinsic pseudocapacitor application, J Energy Storage 40 (2021) 102629, https://doi.org/10.1016/j.est.2021.102629.

[28] Y.Y. Chen, Y. Zhang, X. Zhang, T. Tang, H. Luo, S. Niu, Z.H. Dai, L.J. Wan, J.S. Hu, Self-templated fabrication of MoNi4/MoO3-x Nanorod arrays with dual active components for highly efficient hydrogen evolution, Adv. Mater. 29 (2017) 1–7, https://doi.org/10.1002/adma.201703311.

[29] P. Sivakumar, M.G. Jung, C.J. Raj, H.S. Park, Synergistic integration of three-dimensional architecture composed of two-dimensional nanostructure ternary metal oxide for high-performance hybrid supercapacitors, Int. J. Energy Res. 45 (2021) 21170–21181, https://doi.org/10.1002/er.7170.

[30] M. Yu, H. Liang, R. Zhan, L. Xu, J. Niu, Sm-doped g-C3N4/Ti3C2 MXene heterojunction for visible-light photocatalytic degradation of ciprofloxacin, Chin. Chem. Lett. 32 (2021) 2155–2158, https://doi.org/10.1016/j.cclet.2020.11.069.

[31] H. Salari, J. Shabani Shayeh, A unique 3D structured NiMoO4/MoO3Heterojunction for enhanced supercapacitor performance, Energy Fuels 35 (2021) 16144–16151, https://doi.org/10.1021/acs.energyfuels.1c01793.

[32] F. Nti, D.A. Anang, J.I. Han, Facilely synthesized NiMoO4/CoMoO4 nanorods as electrode material for high performance supercapacitor, J. Alloys Compd. 742 (2018) 342–350, https://doi.org/10.1016/j.jallcom.2018.01.289.

[33] Y. Chen, W. Gu, L. Tan, Z. Ao, T. An, S. Wang, Photocatalytic H2O2 production using Ti3C2 MXene as a non-noble metal cocatalyst, Appl. Catal. Gen. 618 (2021) 118127, https://doi.org/10.1016/j.apcata.2021.118127.

[34] T. Cai, L. Wang, Y. Liu, S. Zhang, W. Dong, H. Chen, X. Yi, J. Yuan, X. Xia, C. Liu, S. Luo, Ag3PO4/Ti3C2 MXene interface materials as a Schottky catalyst with enhanced photocatalytic activities and anti-photocorrosion performance, Appl. Catal. Environ. 239 (2018) 545–554, https://doi.org/10.1016/j.apcatb.2018.08.053.

[35] S. Wang, J. Zhu, X. Wu, L. Feng, Microwave-assisted hydrothermal synthesis of NiMoO4 nanorods for high-performance urea electrooxidation, Chin. Chem. Lett. 33 (2022) 1105–1109, https://doi.org/10.1016/j.cclet.2021.08.042.

[36] S.D. Rani, R. Ramachandran, S. Sheet, M.A. Aziz, Y.S. Lee, A.G. Al-Sehemi, M. Pannipara, Y. Xia, S.Y. Tsai, F.L. Ng, S.M. Phang, G.G. Kumar, NiMoO4 nanoparticles decorated carbon nanofiber membranes for the flexible and high performance glucose sensors, Sens. Actuators B 312 (2020) 127886, https://doi.org/10.1016/j.snb.2020.127886.

[37] S. Nangan, Y. Ding, A.Z. Alhakemy, Y. Liu, Z. Wen, Hybrid alkali-acid urea-nitrate fuel cell for degrading nitrogen-rich wastewater, Appl. Catal. Environ. 286 (2021) 119892, https://doi.org/10.1016/j.apcatb.2021.119892.

[38] K.J. Babu, N. Senthilkumar, A.R. Kim, G.G. Kumar, Freestanding and binder free PVdF-HFP/Ni-co nanofiber membrane as a versatile platform for the electrocatalytic oxidation and non-enzymatic detection of urea, Sens. Actuators B 241 (2017) 541–551, https://doi.org/10.1016/j.snb.2016.10.069.

[39] J.K. Yang, K.S. Ha, H.S. Baek, S.S. Lee, M.L. Seo, Amperometric determination of urea using enzyme-modified carbon paste electrode, Bull. Korean Chem. Soc. 25 (2004) 1499–1502, https://doi.org/10.5012/bkcs.2004.25.10.1499.

[40] G. Wang, J. Chen, Y. Li, J. Jia, P. Cai, Z. Wen, Energy-efficient electrolytic hydrogen production assisted by coupling urea oxidation with a pH-gradient concentration cell, Chem. Commun. 54 (2018) 2603–2606, https://doi.org/10.1039/c7cc09653d.

[41] P. Giannozzi, S. Baroni, N. Bonini, M. Calandra, R. Car, C. Cavazzoni, D. Ceresoli, G.L. Chiarotti, M. Cococcioni, I. Dabo, A. Dal Corso, S. De Gironcoli, S. Fabris, G. Fratesi, R. Gebauer, U. Gerstmann, C. Gougoussis, A. Kokalj, M. Lazzeri, L. Martin-Samos, N. Marzari, F. Mauri, R. Mazzarello, S. Paolini, A. Pasquarello, L. Paulatto, C. Sbraccia, S. Scandolo, G. Sclauzero, A.P. Seitsonen, A. Smogunov, P. Umari, R.M. Wentzcovitch, QUANTUM ESPRESSO: a modular and open-source software project for quantum simulations of materials, J. Phys. Condens. Matter 21 (2009), https://doi.org/10.1088/0953-8984/21/39/395502.

[42] F. Meng, M. Seredych, C. Chen, V. Gura, S. Mikhalovsky, S. Sandeman, G. Ingavle, T. Ozulumba, L. Miao, B. Anasori, Y. Gogotsi, MXene sorbents for removal of urea from dialysate: a step toward the wearable artificial kidney, ACS Nano (2018), https://doi.org/10.1021/acsnano.8b06494.

[43] X. Wang, J.P. Li, Y. Duan, J. Li, H. Wang, X. Yang, M. Gong, Electrochemical urea oxidation in different environment: from mechanism to devices, ChemCatChem (2022) 202101906, https://doi.org/10.1002/cctc.202101906.